Identifying the Origin and Contribution of Surface Storage in TiO_2(B) Nanotube Electrode by In Situ Dynamic Valence State Monitoring

Yuxin Tang, Yanyan Zhang, Oleksandr I. Malyi, Nicolas Bucher, Huarong Xia, Shibo Xi, Zhiqiang Zhu, Zhisheng Lv, Wenlong Li, Jiaqi Wei, Madhavi Srinivasan, Armando Borgna, Markus Antonietti, Yonghua Du,* and Xiaodong Chen*

Monoclinic TiO_2(B) is one of the most promising anode materials for high-rate performance lithium-ion batteries as it possesses the largest theoretical capacity among titania polymorphs. However, fundamental insight into the surface charging mechanism of TiO_2(B) nanomaterials is limited due to the complicated nature of lithiation behavior, as well as the limitations of available characterization tools that can directly probe surface charging process. Here, an in situ approach is reported to monitor the dynamic valence state of TiO_2(B) nanotube electrodes, which utilizes in situ X-ray absorption spectroscopy (XAS) to identify the origin and contribution of surface storage. A real-time correlation is elucidated between the rate-dependent electrode performance and dynamic Ti valence-state change. A continuous Ti valence state change is directly observed through the whole charging/discharging process regardless of charging rates, which proves that along with the well-known non-faradaic reaction, the surface charging process also originates from a faradaic reaction. The quantification of these two surface storage contributions at different charging rates is further realized through in situ dynamic valence state monitoring combined with traditional cyclic voltammetry measurement. The methodology reported here can also be applied to other electrode materials for the real-time probing of valence state change during electrochemical reactions, the quantification of the faradaic and non-faradaic reactions, and the eventual elucidation of electrochemical surface charging mechanisms.

Monoclinic TiO_2(B) is a promising anode material for high-rate and long-lasting lithium-ion batteries (LIBs) as it is characterized by the largest theoretical capacity (335 mAh g^{-1}) among titania polymorphs and small volume expansion (<5%) upon cycling.[1] Despite these advantages, the high-rate performance of TiO_2(B) remains limited by sluggish charge carrier transport,[1c,d,2] thus inspiring much research efforts toward solving the inherent problems of poor electronic conductivity (10^{-13} –10^{-9} S cm^{-1}) and low Li-ion diffusivity (10^{-12}–10^{-9} cm^2 s^{-1}).[1f–l] For example, theoretical modeling[3] has been used provided new insights into the lithiation thermodynamics and kinetics of TiO_2(B) materials, in order to guide the materials design.[4] Numerous TiO_2(B)-based nanostructures and composites have also been fabricated in order to improve charge carrier transport and the overall electrochemical performance.[5]

Despite fruitful progress being made toward the design of TiO_2(B) electrodes, current understanding on the lithiation mechanisms of nanostructured TiO_2(B) remains limited by the complexity of electrochemical reactions in nanostructured materials and poor knowledge on the origin of surface storage.[3–5] Taking a typical discharging process (Scheme 1a) for example, the discharging behavior of the TiO_2(B) nanotube electrode is more complicated (Scheme 1b) than the signature lithiation plateau

Dr. Y. Tang, Dr. Y. Zhang, Dr. H. Xia, Dr. Z. Zhu, Z. Lv, W. Li, J. Wei, Prof. M. Srinivasan, Prof. X. Chen
Innovative Centre for Flexible Devices (iFLEX)
School of Materials Science and Engineering
Nanyang Technological University
50 Nanyang Avenue, Singapore 639798, Singapore
E-mail: chenxd@ntu.edu.sg
Dr. O. I. Malyi
Centre for Materials Science and Nanotechnology
Department of Physics
University of Oslo
P.O. Box 1048 Blindern, NO-0316 Oslo, Norway
The ORCID identification number(s) for the author(s) of this article can be found under https://doi.org/10.1002/adma.201802200.

DOI: 10.1002/adma.201802200

Dr. N. Bucher
Technische Universität München
85748 Garching, Germany
Dr. N. Bucher, Prof. M. Srinivasan
TUM CREATE
Singapore 138602, Singapore
Dr. S. Xi, Dr. A. Borgna, Dr. Y. Du
Institute of Chemical and Engineering Sciences
1 Pesek Road, Jurong Island, Singapore 627833, Singapore
E-mail: du_yonghua@ices.a-star.edu.sg
Prof. M. Antonietti
Department of Colloid Chemistry
Max Planck Institute of Colloids and Interfaces
Potsdam, Germany

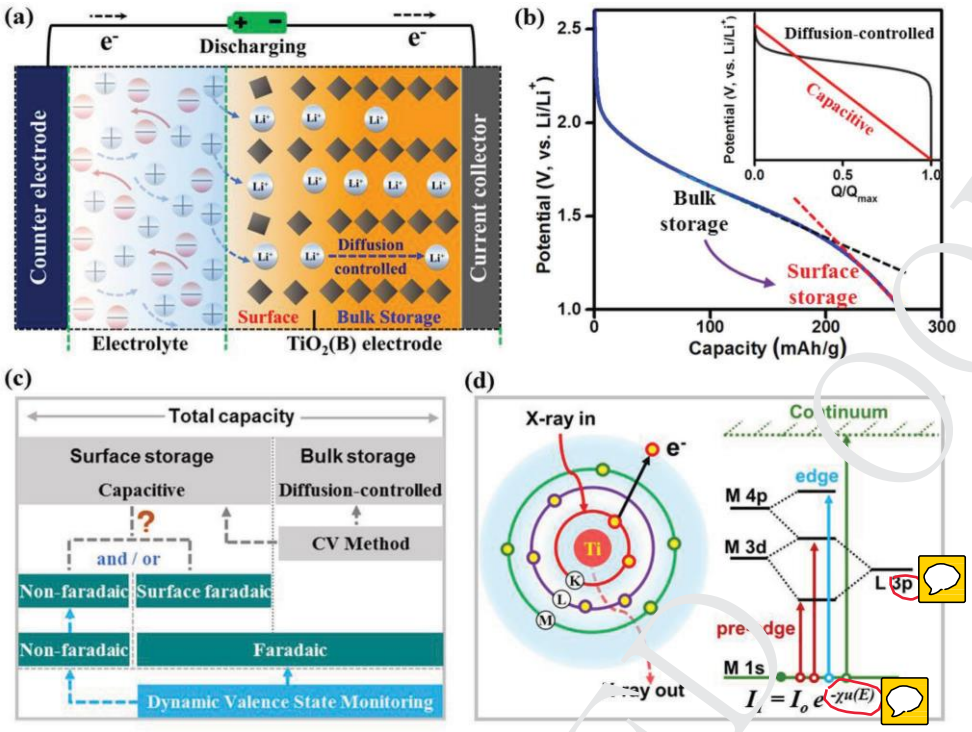

Scheme 1. The current challenge in identifying surface storage contributions for the TiO_2(B) electrode. a) Schematic of the working principle of half-cell LIBs under discharging, where Li-ions are inserted into TiO_2(B) electrode (orange) and Li foil serves as the counter electrode. The electrolyte is composed of solvated Li^+ cations and PF^{6-} anions. b) Typical discharging profile for a prototype TiO_2(B) nanotube electrode, showing the transition from bulk to surface storage. The surface and bulk storage in a,b) are classified based on reaction kinetics with their discharging characteristics shown in the inset of (b). Q/Q_{max} is the efficiency of discharge. c) Schematic of our proposed solution to address the surface charge contributions by in situ dynamic valence state monitoring. Diffusion-controlled bulk storage and capacitive surface storage can be quantified by CV kinetic analysis method. The non-faradaic and faradaic reaction related to Ti valence state change can be quantified from dynamic valence state monitoring. d) Working principle of XAS technique (left) for measuring Ti K-edge absorption energy based on photoelectric effect (right). I_0 and I_1 are X-rays intensity before and after transmitting through the sample, respectively; x is the sample thickness.

of anatase TiO_2 and $Li_4Ti_5O_{12}$.[5a–i] Specifically, two linear discharging slopes (dotted line, Scheme 1b) in sequence would be observed, which originate from diffusion-controlled bulk insertion and capacitive surface storage (inset in Scheme 1b), and are classified based on reaction kinetics.[6] It is clear that Li-ion insertion in bulk TiO_2 reduces Ti valence state (reduction process) during discharging. As shown in Scheme 1c, surface storage is generally associated with both non-faradaic and/or surface faradaic reactions (the latter also termed as pseudocapacitive).[7] However, for TiO_2(B) nanotube electrodes, the origin of surface storage (Scheme 1b,c) from non-faradaic and/or surface faradaic reactions is still unknown. Although previous studies[8] have reported valence state measurements in titania materials, continuous monitoring of the valence state change and dynamic measurements under various charging/discharging rates are still lacking, rendering difficult to identify the origin of the surface storage. In addition, although the cyclic voltammetry (CV) kinetic analysis method[6a,b] (see discussion in Supporting Notes, Supporting Information) can quantitatively determine the contribution of capacitive and diffusion-controlled reactions (Scheme 1c) toward total capacity, the contribution of surface storage (including non-faradaic and surface faradaic reactions) is still not quantified in battery systems. Previous works[7a,9] showed that while non-faradaic capacity can be estimated by electrochemical methods (CV and electrochemical impedance spectroscopy), these attempts were limited to supercapacitor configuration and cannot represent the real case in LIBs. It is difficult to directly identify surface charging process with conventional techniques due to the complicated nature of lithiation behavior, low X-ray scattering power of lithium atoms, and poor crystallinity of lithiated TiO_2(B) nanomaterials.[1c,2d] Therefore, the development of new methodologies to characterize the electrochemical surface charging process in situ is crucial toward understanding the surface charging mechanism, as well as achieving high-rate performance with nanostructured TiO_2(B).[1e,10]

The faradaic reaction refers to a charge-transfer process that results from electrochemical redox reaction related to changes in the Ti valence state.[11] Therefore, we hypothesized that the origin and contribution of surface storage from faradaic and/or non-faradaic reactions (Scheme 1c) in TiO_2(B) would be identified via continuous monitoring of the Ti valence state change during charging/discharging. To achieve this, a characterization tool capable of continuous real-time monitoring of valence state change under different charging/discharging rates would be highly desired. It is known that XAS probes the X-ray absorption coefficient $\mu(E)$ of the absorbing atom (Scheme 1d) modulated by its surrounding atoms through

the photoelectric effect.[11] XAS consists of the X-ray absorption near-edge structure (XANES) and extended X-ray absorption fine structure (EXAFS). XANES can determine the valence state of an atom in the compound while EXAFS can elucidate local chemical environment of the atom, including coordination numbers, distances, and species of the neighbors around the absorbing atom.[11c] Moreover, hard X-ray XAS for Ti-K edge does not require the sample to possess high crystallinity, and can penetrate deeply in the matter (>20 µm) to gain the average signal.[11d] These merits render the XAS technique a promising tool to verify our hypothesis.

Herein, we used an in situ XAS technique capable of tracking real-time Ti valence state change at different charging/discharging rates to identify the origin and contribution of surface charge storage in a prototype TiO_2(B) nanotube electrode. It is revealed that the Ti valence state changes continuously throughout the charging/discharging process, which confirms that the surface storage originated from both surface faradaic and non-faradaic reactions simultaneously, regardless of charging rates. Operando X-ray diffraction (XRD) also proved that the surface faradaic reaction is characterized by continuous anisotropic expansion of crystal planes of Li_xTiO_2(B) during lithiation. According to our theoretical calculations, the surface faradaic reaction causes the discharging behavior to change due to an increase of Li-ion insertion site energy at the surface (Scheme 1b). Furthermore, through the in situ dynamic valence state monitoring with the CV kinetic analysis method, the non-faradaic capacity (≈18.2 mAh g^{-1}) and surface faradaic capacity at different charging rates are quantified. It can be observed that the ratio of capacity contribution from surface storage increases with the increase of charging rates. The current findings of the surface storage mechanism have implications for insertion-type compounds in general, which offers the potential to guide the enhancement of electrode performance.

The first step of our mechanistic studies is the proof-of-concept, in which we verified the feasibility of using in situ XAS (Figure 1) to probe the non-faradaic and faradaic reactions during lithiation. Real-time monitoring of the Ti valence state and atomic structure changes by in situ XAS was conducted on a binder-free TiO_2(B) electrode in our customized battery cell (Scheme S1, Supporting Information). The unique elongated TiO_2(B) nanotube (Figure S1, Supporting Information) was an ideal binder-free electrode system for precisely elucidating the surface charging mechanism, since a binder on the electrode materials surface would influence the non-faradaic reaction.[5c,j] A stable galvanostatic charging/discharging profile with a nearly constant slope was observed for TiO_2(B) nanotube electrode (Figure 1a). During discharging, the absorption edge of Ti K-edge XANES spectra was monotonically shifted to lower energy (Figure 1b), corresponding to a continuous reduction of the average Ti valence state. This shift was caused by the transition of Ti^{4+} to Ti^{3+} in Li_xTiO_2(B) during lithiation. Correspondingly, the C1 and C2 crests (the signature of Ti–O interaction) shown in Figure 1b shifted to lower energy upon Li-ion insertion. These two crests can be attributed to

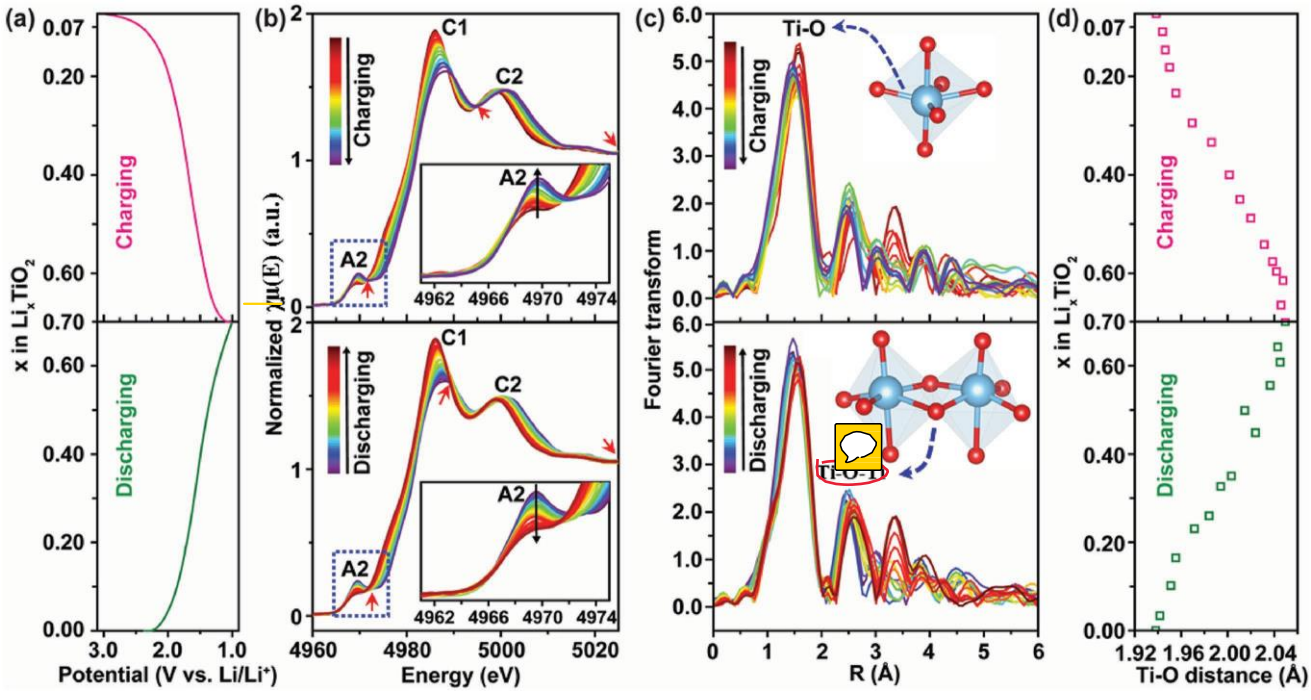

Figure 1. In situ XAS studies of the stabilized TiO_2(B) nanotube electrode at a low current density of 0.075 A g^{-1}. a) Stable lithiation and de-lithiation profile after three discharging/charging cycles. The corresponding b) XANES and c) EXAFS stacking absorption spectra of Ti K-edge for tracking of the structural evolution during discharging/charging processes. During discharging, the absorption edge of Ti K-edge XANES spectra is monotonically shifted to lower energy, corresponding to a continuous reduction of average Ti valence state. The insets in (b) are the zoom-in images taken from the square area in (b). The quasi-isosbestic points in (b) are indicated by red arrows. d) Evolution of Ti⊗O atomic distance upon discharging/charging. A gradual expansion of the Ti⊗O bond length is found upon discharging, which is due to the formation of larger radius for Ti^{3+} (0.67 Å) during Li-ion insertion.

the electronic dipole transition from the core Ti 1s orbital to an unoccupied Ti orbital,[8b] and the increased intensity of the C1 peak should be due to the increased anisotropic orientation of Ti⊗O bond.[12] As for the preedge feature, only one peak marked as "A2" (related to dipolar electronic transitions from Ti 1s to e_g levels)[8b,13] was seen (Figure 1b) for the stabilized TiO_2(B) electrode after cycling, in contrast to the three pre-edge peaks (A1–A3) of the pristine TiO_2(B) electrode (Figure S2, Supporting Information). Their origins and transformations are discussed in Figure S2 (Supporting Information). During discharging, the A2 peak intensity first decreases due to structural distortion upon Li-ion insertion. The intensity then increases slightly after the formation of $Li_{0.55}TiO_2$(B) at the end of lithiation process, which can be associated with the presence of the more regular TiO_6 octahedra.[13] This behavior may be due to the rearrangement of Li-ion sites in the crystal or the change of the Li-ion diffusion pathway.

Having established our proof-of-concept, the local structure evolution upon charging/discharging was then probed in situ by Ti K-edge EXAFS. Fourier transformation of EXAFS oscillations provided the radial distribution from individual shells of neighboring atoms around Ti atom, as shown in Figure 1c. The three peaks located at about 1.5, 2.5, and 3.3 Å originated from six coordinated Ti⊗O bonds in the TiO_6 octahedra, first neighbors of five coordinated Ti–Ti (edge) scattering, and third neighbors of four coordinated Ti–Ti (corner) scattering, respectively.[8b] During discharging, the peak intensity from Ti⊗O bonds would first gradually decrease, then increase at the end state. This behavior indicates the increased distortion of the TiO_6 octahedra during continuous Li-ion insertion. While reaching a lithiated phase of $Li_{0.55}TiO_2$(B), the crystal structure would become less disordered, which agrees with the observed A2 peak change. To quantify Ti⊗O bond length for the first shell (Figure 1d), we performed the fitting of radial distribution data in Figure 1c by the Artemis software.[14] To reduce the ambiguity of the fitting, the coordination number for Ti was fixed to six to minimize variable parameters. A small R-factor (≈0.01, Table S1, Supporting Information) was obtained, which indicated excellent fitting for the bond length. According to the fitting result, gradual expansion of the Ti⊗O bond length occurred upon discharging. This structural change was due to Li-ion insertion, resulting in the formation of Ti^{3+} with larger radius (0.67 Å) than that of Ti^{4+} (0.61 Å).[15] The change of the bond length was not obvious at the beginning and end of the lithiation process (Figure 1d), which suggested limited Li-ion bulk insertion. After charging, both the local atomic structure (Figure 1c) and bond length (Figure 1d) were reversibly returned to the original state, indicating the rigid and stable structure of TiO_2(B).

An issue that we have to address next is that fast charging of LIBs may impede the application of in situ XAS to monitor the dynamic valence state change. Specifically, the recording time is long (≈5 min) for a full XAS spectrum (XANES and EXAFS) with an energy ~~range~~ of ≈500 eV (corresponding to an energy scanning rate of 100 eV min^{-1}), which would result in limited collected data points for a charging or discharging process. To address this issue, we shortened the record time to 0.5–2 min for the XANES measurement only, with a narrowed energy ~~range~~ of 50–100 eV and an increased energy scanning rate (100–200 eV min^{-1}). With this approach, the rate-dependent charge storage contribution and Ti valence states were revealed and quantified at different charging/discharging rates (Figure 2

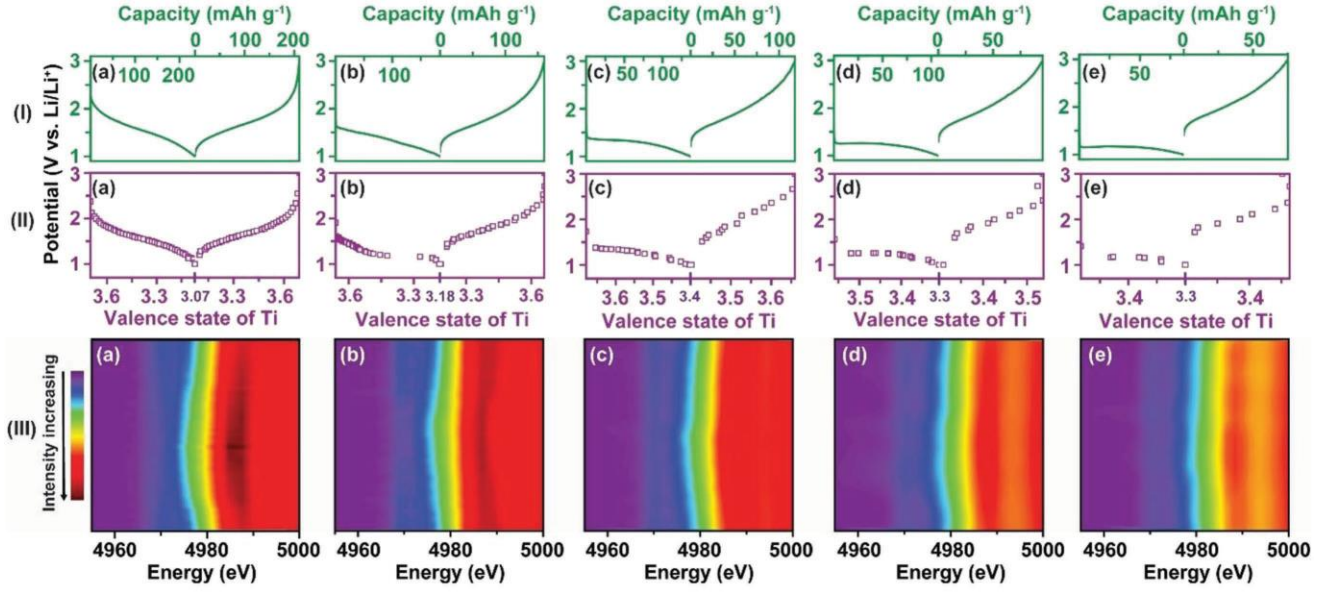

Figure 2. In situ dynamic valence state monitoring approach: Dependence of Ti valence state evolution on the charging/discharging capacity at various current densities of a) 0.075, b) 0.45, c) 0.9, d) 1.25, and e) 1.75 A g^{-1}. (I) Galvanostatic discharging/charging profiles of TiO_2(B) nanotube electrode. (II) The synchronously progressive valence state change of Ti element. The valence state evolution curves match well with the charging/discharging curves at different charging currents, indicating that the charging behavior is mainly affected by the faradaic reaction into TiO_2(B). (III) The corresponding 2D contour plots of the Ti K-edge ~~energy~~ of TiO_2(B) nanotube electrode under different discharging/charging currents. Upon discharging, Ti-K absorption edge (4975–4985 eV) in contour plot is shifted to lower energy at different discharging rates. While at high current density, the change of the absorption edge is less pronounced. The Ti K-edge adsorption energy is normalized for the comparison.

and Figure S3, Supporting Information). Correspondingly, the correlation between electrode performance (Figure 2I) and average Ti valence state (Figure 2II) was evaluated on the same cell by in situ dynamic valence state monitoring. The corresponding 2D contour plots derived from in situ XANES spectra for TiO_2(B) are shown in Figure 2III and Figure S4 (Supporting Information). Upon discharging, Ti-K absorption edge (4975–4985 eV) in the contour plot (Figure 2III) was shifted to lower energy at different charging rates. At high current density, the change of the absorption edge was less pronounced (Figure 2III-d,e, and Figures S3 and S4, Supporting Information). This observation is consistent with the lower capacity achieved at high rates. Upon charging, the absorption edge can return to the original state upon lithium extraction regardless of the charging rates, indicating the good reversibility of the TiO_2(B) structure during cycling.

Although the contour plots can provide us with a visual impression of in situ valence state change, quantitative data are required to deduce the factors that contribute to the charge storage. The total storage capacity can be divided into faradaic capacity, which originated from the change of Ti valence state, and non-faradaic capacity, which is attributed to other contributions. Herein, linear combination fitting (LCF, see discussion in Supporting Notes, Supporting Information) was applied based on the appearance of quasi-isosbestic points[12,16] in Figure 1b (red arrows). According to our analysis, each intermediate state of the Ti XANES spectrum curve can be well fitted by a linear combination of the corresponding XANES spectra of the lowest and highest valence states,[16a] which correspond to the fully lithiated and initial states, respectively. The average Ti valence states in initial and lithiated states were first determined from the absorption edge shift (Figure S5, Supporting Information) relative to the edge position, which was defined by the interception of the spectrum at half of the normalized intensity.[16b] The expected uncertainty to determine the average Ti valence state by this approach was about ±5%.[16a,c] The edge shift for per valence state was determined to be 5.01 eV from fresh TiO_2(B) and Ti_2O_3 as a standard reference sample (Figure S5b, Supporting Information), which was consistent with the literature value.[13,17] Taking this result into account, we established the Ti average valence state in the initial states of stabilized TiO_2(B) after cycling and lithiated TiO_2(B) to be $Ti^{3.70+}$ and $Ti^{3.07+}$, respectively, at a current density of 0.075 A g^{-1} (Figure S5c,d, Supporting Information). After obtaining the two end states of the Ti valence state, we can obtain a precision better than 1% when using LCF to determine variations in the relative ratio of Ti^{3+} and Ti^{4+} during different states of charge (Table S2, Supporting Information). A typical fitting result was plotted in Figure S6 (Supporting Information) for a current density of 0.075 A g^{-1}, and all of the LCF fittings matched well with the experimental results. By the same method, the fitting for high current densities was conducted, and the fitting data also matched perfectly with the experimental data (Figures S7–S10, Supporting Information). The fitting details for each intermediate state at different charging/discharging rates and detailed discussion are provided in Tables S2–S6 (Supporting Information) and Supporting Notes (Supporting Information), respectively.

The corresponding valence state for each charging/discharging state would be combinations of different fractions of Ti^{4+} and Ti^{3+}, as shown in Figure S11 (Supporting Information). By summing up each valence state multiplied by their corresponding fractions, the average Ti valence state at each charging/discharging state under different charging rates was obtained, as shown in Figure 2II. Four distinct characteristics were observed for dynamic evolution of the Ti valence state. First, the valence state evolution curves matched well with the charging/discharging curve at different charging currents, which indicated that the charging capacity and behavior were mainly affected by the faradaic reaction within the TiO_2(B) lattice. Second, Ti valence state changed throughout the charging/discharging process although smaller rates of change were observed at the beginning and the end of the discharging/charging process, which indicated that the faradaic reaction was also occurring during surface storage. Third, the total valence state change dramatically decreased with increased charging rates, which was consistent with the rate-dependent performance. Fourth, the initial valence state of Ti decreased at higher current densities. This can be attributed to the continuous mode of in situ XAS measurement with a gradual and sequential increase of current density. At a small charging density (≤0.9 A g^{-1}), the valence state could be easily returned to the initial value ($Ti^{3.7+}$), while at a higher current density (≥1.25 A g^{-1}), the electrode system suffered from larger reaction polarization, leading to significant reduction in electrode performance (mainly from the faradaic reaction). Due to the limited Li-ion diffusion kinetics, the increase of charging rate would not allow complete removal of Li-ion from the sample, resulting in the stabilization of lower initial Ti valence states. Therefore, further Li-ion insertion would reduce valence state from the new initial value.

To obtain further insights into the crystal structure evolution during lithiation and its correlation with lithiation-induced valence state change, we performed operando XRD study on the insertion/deinsertion of Li ions into/from TiO_2(B) (Figure 3a,b). Three main reflections at 28.6°, 43.6°, and 47.9° were observed, which corresponded to the (002), (003), and (020) crystal planes of TiO_2(B),[8c] respectively. Quantitative data on the real-time change of atomic/plane arrangement was obtained by analyzing the shift of the peak position and intensity. Upon discharging, the above three peaks were gradually shifted to lower reflection angles (Figure 3c,e,h), indicating plane expansion during lithiation. These monotonically left-shifted peaks indicated single-phase reaction without apparent phase changes. The quantitative data on the (002) and (020) peak change is shown in Figure 3f,i, respectively. The degree of crystal disorder was estimated by comparing the diffraction intensity of the (002) peak with the constant diffraction intensity of the Al (111) plane (Figure 3b). The ratio of $I_{TiO2(B)(002)}/I_{Al(111)}$ decreased during discharging and gradually increased during charging. This behavior indicated that the degree of crystal disorder of the atomic arrangement on the (002) plane was degraded during discharging (Figure 3g). Upon charging, these characteristic peaks and their intensities could be recovered to the initial charged state. The structure evolution revealed by XRD was consistent with the in situ

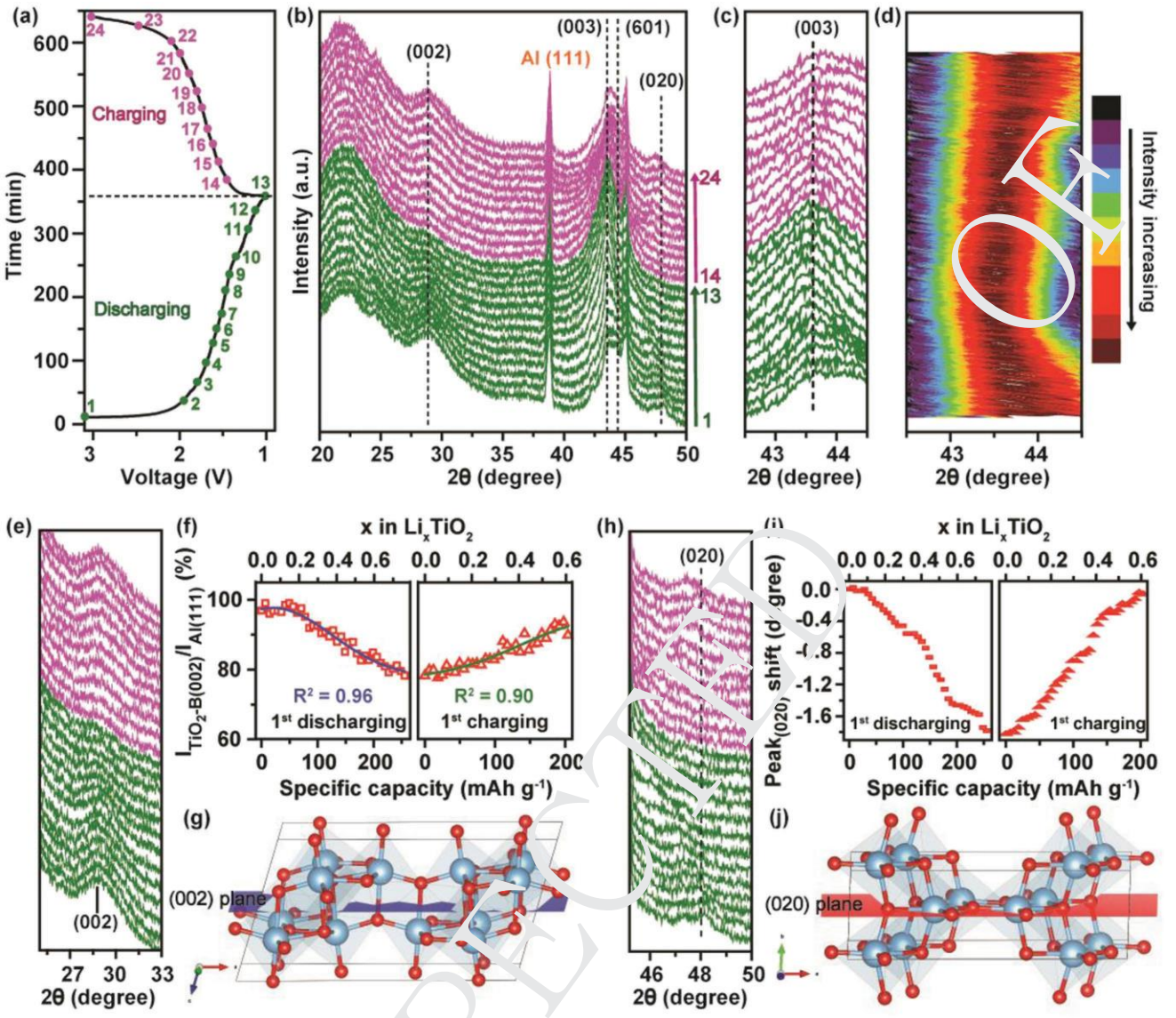

Figure 3. Operando XRD analysis of TiO_2(B) nanotube electrode under discharging/charging at a current density of 0.06 A g^{-1}. a) Galvanostatic discharging/charging curves. b) Operando XRD patterns of TiO_2(B) electrode at different stages that points 1–13 represent the discharging process and points 14–24 represent the charging process. c) Magnified (003) peak and d) its corresponding 2D contour plots. e) Magnified (002) peak and f) its corresponding XRD peak intensity change during discharging/charging. g) The (002) plane of TiO_2(B) stacked along the *c*-axis (red: oxygen atoms; blue: titanium atoms). h) Magnified (020) peak and i) its corresponding peak shift during discharging/charging. j) The (020) plane of TiO_2(B) stacked along the *b*-axis.

XAS measurement (Figure 1d). In particular, a more obvious peak shift was observed in (020) plane compared to that in the other two crystal planes (Figure 3h,i). This finding is reasonable since Li-ion diffusion through the (020) plane with open channels along the b-axis (Figure 3j) has the lowest migration energy barrier.[1c,7d] The increase in the degree of peak shift was observed when the mole fraction of stored lithium (Li_x) was between 0.1 and 0.6 during discharging. Beyond this region, the degree of peak shift was much smaller (Figure 3i). This region matched well with the lithiation/delithiation potential window (1.4–1.8 V) of TiO_2(B), and the peak shift beyond this region was smaller, corresponding to the evolution of Ti valence state. To further understand the full picture of lithiation process, we correlated the real-time evolution of Ti valence state with crystal structure change (Figure S12, Supporting Information). We have found that the real-time evolution of the change in XRD peak shift follows a slope similar to that of the XAS-derived Ti valence state during charging/discharging, which further proved that the full faradaic process occurred with a continuous (002)/(020) plane expansion (Figure 3e,h, Figure S12, Supporting Information) even during surface storage. In addition, three important steps for Li-ion migration into TiO_2(B), namely surface adsorption, bulk insertion, and surface storage, are proposed in Figure S12 (Supporting Information) with detailed discussion. Herein, the operando XRD result has proven the solid-solution reaction during lithiation. The absent phase transition

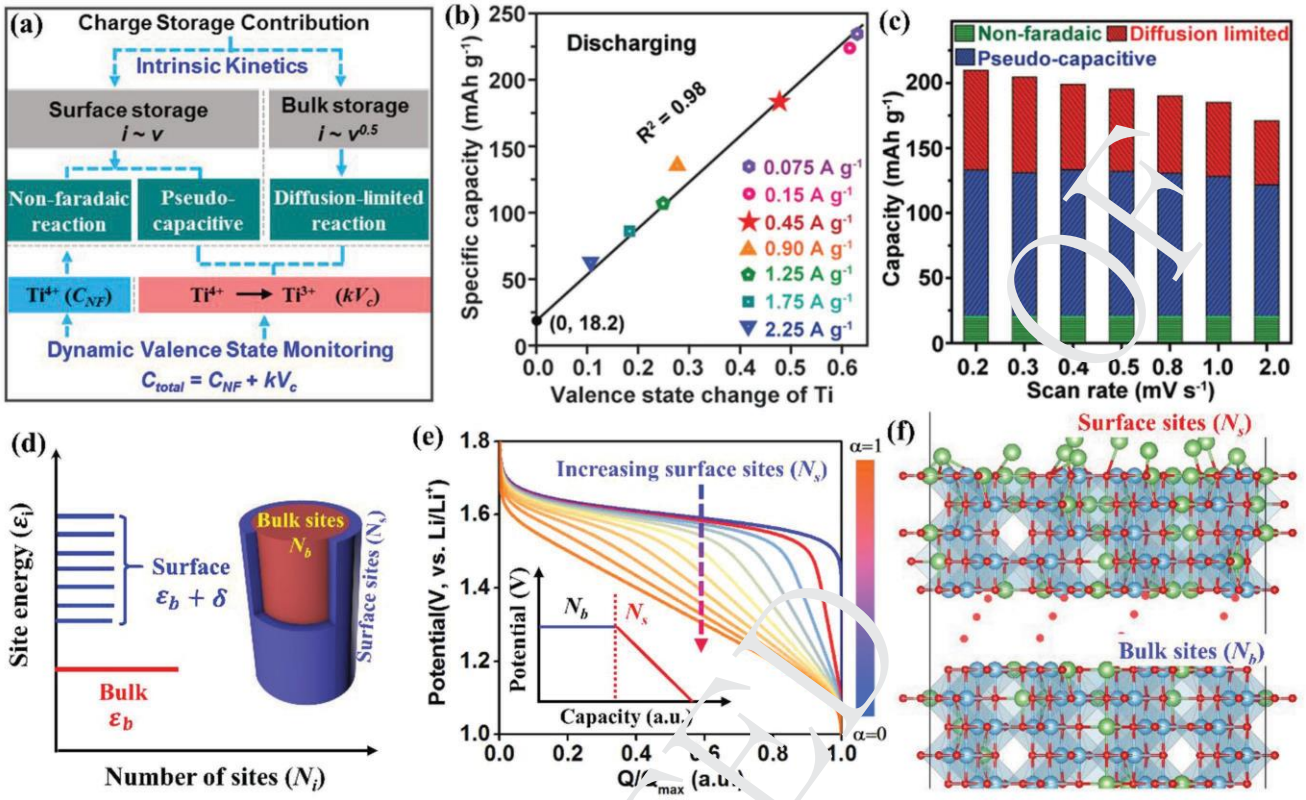

Figure 4. Identification of surface charge contributions for TiO_2(B) nanotube electrode and theoretical modeling of Li-ion insertion site energy. a) Dynamic valence state monitoring to reveal the surface charging contribution combining with CV kinetic analysis. b) Correlation of the specific capacity with Ti valence state at varied current rates, giving non-faradaic reaction capacity from *y*-intercept. c) Diffusion-limited, pseudo-capacitive, and non-faradaic capacitive contributions to the total capacity at different scan rates. d) The correlation of Li-ion site energy (ε) with the number of the site (N_i). Distribution of the site energy for bulk materials (ε_b, red line) with surface sites considered ($\varepsilon_b + \delta$, blue line), resulting in the decrease of discharging potential shown in the inset of (e). e) Calculated discharge profiles with different ratios of surface sites (α = 0–1.0) by modified lattice-gas model. Here, the typical values are set as: $\varepsilon_b = -1.6$ eV, $\delta = 0.5$ eV, $k = 1.38 \times 10^{-23}$ J K^{-1}, $T = 298.15$ K. The inset in (e) is the scheme for bulk sites (N_b) and surface sites (N_s) for TiO_2(B). f)Schematic illustration of Li occupations for surface sites (top) including Li surface adsorption and insertion, and bulk sites (bottom) with diffusion-limited insertion in TiO_2(B) (010) surface. During lithiation, Li concentration decreases from surface layers to bulk sites.

with small structural rearrangements and volume changes is the key to realize fast charging (which will be discussed later in Figure S15, Supporting Information) for the TiO_2(B) electrode.

To explore the origin of rate-dependent capacity contributions (Figure 4a), we quantitatively identified each capacity contribution through the dynamic valence state monitoring with the kinetic analysis by traditional CV measurements, which can differentiate the contributions of the capacitive and diffusion-controlled reactions (see discussion in Supporting Notes, Supporting Information). The capacitive reaction on the electrode surface consists of non-faradaic and surface faradaic (pseudocapacitive) reactions. From the electrochemical perspective, the total capacity should be composed of non-faradaic contribution (C_{NF}) and faradaic contribution (C_F) related to the Ti valence state change. Theoretically, C_F should be proportional to the valence state change (V_c), and C_{NF} should be nearly constant at wide charging rates before reaching kinetic limit by electrostatic adsorption. To prove this, we explored the correlation of specific capacity with Ti valence state change (Figure 4b). As we expected, the total capacity (C_{total}) showed a linear relationship with V_c at different charging rates

$$C_{total} = C_{NF} + C_F = C_{NF} + kV_c \quad (1)$$

in which, k value is related to the theoretical capacity per valence state change. Based on the Equation (1), C_{NF} from the intercept is ≈18.2 mAh g. This value was comparable to that found from our theoretical evaluation (see discussion in Supporting Notes, Supporting Information). To quantitatively obtain each capacity contribution, the capacitive and diffusion-controlled capacities were first calculated from kinetic analysis by CV measurement. The typical CV curve and its derived data for TiO_2(B) anode with various scanning rates are included in Figure S13 (Supporting Information). To identify the contribution of the capacitive reaction, the relationship between the CV current (i) and scan rate (v) was analyzed via $i = av^b$. The b value of 0.5 would corresponds to diffusion-controlled behavior, and 1.0 would indicate capacitive process.[7] It was found that the b value for anodic peaks is 0.82 (Figure S13, Supporting Information) for the TiO_2(B) nanotube electrode, indicating mixed contribution from the diffusion and capacitive reactions. Contribution fractions between the aforementioned two reactions at higher scan rates were also quantified

(Figure S13, Supporting Information). Here, it was assumed that C_{NF} determined by various galvanostatic charging rates (Figure 4b) would be identical to that of C_{NF} obtained by CV measurements. By subtracting the contribution from the C_{NF}, we can build the correlation between the diffusion-controlled, pseudocapacitive, and non-faradaic capacitive contributions, as shown in Figure 4c. The results showed minor changes in the pseudocapacitive capacity at slow scanning rates, and slight decreases at high scanning rates (2 mV s^{-1}), while the diffusion-controlled capacity continuously decreased with increasing scanning rates. The continuous decrease was more obvious at higher scanning rates of 20 mV s^{-1} (detailed discussion in Figure S14, Supporting Information). Based on the quantification, the capacity contribution percentage for non-faradaic, pseudocapacitive, and diffusion-controlled capacity changed from 9%, 49%, 42% to 11%, 60%, 29%, respectively, when a scanning rate increased from 0.2 to 2.0 mV s^{-1}. These results showed that the capacity contribution ratio of surface storage (non-faradaic and pseudocapacitive reactions) increased with the increase of charging rates. The capacity of the surface reaction was dominant at fast charging rates (Figure 4c and Figures S13 and S14, Supporting Information), which was mainly due to the high surface area of TiO_2(B) nanotubes (≈163 m^2 g^{-1}). Indeed, we demonstrated that the TiO_2(B) nanotubes possessed higher charge storage capacity than that of TiO_2(B) nanowires (with a surface area ≈25 m^2 g^{-1}) at a wide scanning rate (Figure S15, Supporting Information). In a plot of charge capacity versus $v^{-1/2}$, linear regions would indicate diffusion-limited capacity, while capacitive contribution would be independent of the scanning rate.[7c] Clearly, the charge storage mechanism was mainly diffusion-limited for TiO_2(B) nanowires at a high scanning rate of 20 mV s^{-1} (Figure S15a, Supporting Information), while TiO_2(B) nanotubes still possessed high charge capacity that was mainly attributed to the enriched surface storage reaction (Figure S15b, Supporting Information). Therefore, it is important to design nanostructure electrodes with maximized surface storage and Li-ion diffusivity to enhance bulk insertion.

To further understand the role of surface storage during the charging/discharging process, we modeled the discharging behavior by modified lattice gas model, in order to predict the Li occupation of active sites in electrodes as a function of lithiation voltage.[18] As TiO_6 octahedra layers for TiO_2(B) nanomaterials at the surface have a disordered structure, compared to the site energy for bulk insertion (ε_b), site energy (ε) fluctuation for Li-ion insertion would be induced. This means that the site energy near the surface can be assumed to be uniformly dispersed to a certain extent ($\varepsilon_b+\delta$, Figure 4d) when compared with ε_b. Based on this, the simulated discharging curves with a different fraction of surface storage (α) derived from the modified lattice gas model (discussion in Supporting Notes, Supporting Information) are shown in Figure 4e as a function of Li site occupancy (x) via

$$x = (1-\alpha)\frac{1}{1+\exp\left(-\frac{\varepsilon_b+eE}{kT}\right)} - \frac{\alpha kT}{\delta}\ln\left[\frac{1+\exp\left(-\frac{\varepsilon_b+\delta+eE}{kT}\right)}{1+\exp\left(-\frac{\varepsilon_b+eE}{kT}\right)}\right] \quad (2)$$

where E is the open-circuit voltage, T is the temperature, k is the Boltzmann constant, ε_b is the site energy for bulk insertion, and δ is the increased site energy due to surface effect. Our model (Figure 4e) indicated that, for the bulk insertion, the slight ε_b changes at different lithiation voltages were due to the continuous occupations of interstitial Li sites in TiO_2(B). For Li-ion insertion into the surface layers of TiO_2(B), the discharging behavior changed to capacitive with a deeper slope (inset of Figure 4e). This capacitive behavior would be more obvious for the increasing fractions of surface insertion sites (Figure 4e). According to our modeling, the change in discharging profile of TiO_2(B) (Scheme 1b) would be induced by the transition from Li-ion insertion from bulk to surface storage (Figure 4f). This is due to the increase of surface site energy ($\varepsilon_b+\delta$) in the surface faradaic reaction, which agrees with our experimental observation (Figures 2–4).

In summary, an advanced in situ XAS technique capable of tracking dynamic Ti valence state change as a function of Li-ion content at different charging rates was developed to identify the origin and contribution of surface storage to the capacity of the TiO_2(B) nanotube electrode. Through this platform, we proved that the surface storage originated from both the faradaic and non-faradaic reactions regardless of charging rates, and the surface faradaic reaction induces the discharging behavior change, which is due to an increase of Li-ion insertion site energy at the surface according to our theoretical modeling. In addition, through dynamic valence state monitoring with kinetic analysis by the CV method, a quantitative non-faradaic capacity (18.2 mAh g^{-1}) was deduced for TiO_2(B) nanotubes. The non-faradaic, pseudocapacitive, and diffusion-controlled capacities contributed around 11%, 60%, 29% to the total, respectively, at a scanning rate of 2.0 mV s^{-1}, and the ratio of surface storage contribution increased with the increase of charging rates. Our methodology for in situ dynamic valence state monitoring has significant implications for a wide family of electrode materials and other related electrochemical reactions, with regards to real-time observation of valence state changes, quantification of the electrochemical surface reaction, and elucidation of the charging mechanism under fast charging.

Supporting Information

Supporting Information is available from the Wiley Online Library or from the author.

Acknowledgements

This work was supported by Singapore MOE Tier 2 (MOE2015-T2-1-110), Singapore National Research Foundation (Nanomaterials for Energy and Water Management CREATE Programme Phase II) and the Research Council of Norway (ToppForsk project: 251131).

Conflict of Interest

The authors declare no conflict of interest.

Keywords

in situ XAS fast charging, lithium-ion batteries, surface charging mechanism, TiO_2(B) nanotube anode

Received: April 6, 2018
Revised: June 5, 2018
Published online:

[1] a) H. Liu, F. C. Strobridge, O. J. Borkiewicz, K. M. Wiaderek, K. W. Chapman, P. J. Chupas, C. P. Grey, *Science* 2014, *344*, 1252817; b) A. Van der Ven, J. Bhattacharya, A. A. Belak, *Acc. Chem. Res.* 2012, *46*, 1216; c) X. Hua, Z. Liu, M. G. Fischer, O. Borkiewicz, P. J. Chupas, K. W. Chapman, U. Steiner, P. G. Bruce, C. P. Grey, *J. Am. Chem. Soc.* 2017, *139*, 13330; d) Y. Zhang, O. I. Malyi, Y. Tang, J. Wei, Z. Zhu, H. Xia, W. Li, J. Guo, X. Zhou, Z. Chen, C. Persson, X. Chen, *Angew. Chem., Int. Ed.* 2017, *56*, 14847; e) J. B. Goodenough, K. S. Park, *J. Am. Chem. Soc.* 2013, *135*, 1167; f) S. Lee, J. Cho, *Angew. Chem., Int. Ed.* 2015, *54*, 9452; g) H. G. Jung, M. W. Jang, J. Hassoun, Y. K. Sun, B. Scrosati, *Nat. Commun.* 2011, *2*, 516; h) Y. X. Tang, Y. Y. Zhang, J. Y. Deng, J. Q. Wei, H. L. Tam, B. K. Chandran, Z. L. Dong, Z. Chen, X. D. Chen, *Adv. Mater.* 2014, *26*, 6111; i) K. J. Griffith, A. C. Forse, J. M. Griffin, C. P. Grey, *J. Am. Chem. Soc.* 2016, *138*, 8888; j) N. Takami, Y. Harada, T. Iwasaki, K. Hoshina, Y. Yoshida, *J. Power Sources* 2015, *273*, 923; k) V. Aravindan, Y. S. Lee, S. Madhavi, *Adv. Energy Mater.* 2015, *5*, 1402225; l) S. Brutti, V. Gentili, H. Menard, B. Scrosati, P. G. Bruce, *Adv. Energy Mater.* 2012, *2*, 322.

[2] a) J. Maier, *Angew. Chem., Int. Ed.* 2013, *52*, 4998; b) W. Zhang, M. Topsakal, C. Cama, C. J. Pelliccione, H. Zhao, S. Ehrlich, L. Wu, Y. Zhu, A. I. Frenkel, K. J. Takeuchi, E. S. Takeuchi, A. C. Marschilok, D. Lu, F. Wang, *J. Am. Chem. Soc.* 2017, *139*, 16591; c) M. Salanne, B. Rotenberg, K. Naoi, K. Kaneko, P. L. Taberna, C. P. Grey, B. Dunn, P. Simon, *Nat. Energy* 2016, *1*, 16070; d) C. P. Grey, J. M. Tarascon, *Nat. Mater.* 2017, *16*, 45; e) J. Lee, A. Urban, X. Li, D. Su, G. Hautier, G. Ceder, *Science* 2014, *343*, 519; f) L.-P. Yang, X.-J. Lin, X. Zhang, W. Zhang, A.-M. Cao, L.-J. Wan, *J. Am. Chem. Soc.* 2016, *138*, 5916; g) X.-X. Zeng, Y.-X. Yin, N.-W. Li, W.-C. Du, Y.-G. Guo, L.-J. Wan, *J. Am. Chem. Soc.* 2016, *138*, 15825.

[3] a) C. Arrouvel, S. C. Parker, M. S. Islam, *Chem. Mater.* 2009, *21*, 4778; b) A. R. Armstrong, C. Arrouvel, V. Gentili, S. C. Parker, M. S. Islam, P. G. Bruce, *Chem. Mater.* 2010, *22*, 6426; c) A. G. Dylla, P. Xiao, G. Henkelman, K. J. Stevenson, *J. Phys. Chem. Lett.* 2012, *3*, 2015; d) A. S. Dalton, A. A. Belak, A. Van der Ven, *Chem. Mater.* 2012, *24*, 1568.

[4] a) Y. Tang, Y. Zhang, X. Rui, D. Qi, Y. Luo, S. Chen, J. Guo, J. Wei, W. Li, J. Deng, Y. Lai, B. Ma, X. Chen, *Adv. Mater.* 2016, *28*, 1567; b) Z. Lv, Y. Luo, Y. Tang, J. Wei, Z. Zhu, X. Zhou, W. Li, Y. Zeng, W. Zhang, Y. Zhang, D. Qi, S. Pan, X. J. Loh, X. Chen, *Adv. Mater.* 2018, *30*, 1704531; c) Y. Xu, Z. Lin, X. Zhong, X. Huang, N. O. Weiss, Y. Huang, X. Duan, *Nat. Commun.* 2014, *5*, 4554; d) S. Yang, X. Feng, K. Müllen, *Adv. Mater.* 2011, *23*, 3575.

[5] a) M. Zukalová, M. Kalbáč, L. Kavan, I. Exnar, M. Graetzel, *Chem. Mater.* 2005, *17*, 1248; b) Y. Ren, Z. Liu, F. Pourpoint, A. R. Armstrong, C. P. Grey, P. G. Bruce, *Angew. Chem., Int. Ed.* 2012, *51*, 2164; c) Y. Tang, Y. Zhang, J. Deng, D. Qi, W. R. Leow, J. Wei, S. Yin, Z. Dong, R. Yazami, Z. Chen, X. Chen, *Angew. Chem., Int. Ed.* 2014, *53*, 13488; d) S. Liu, Z. Wang, C. Yu, H. B. Wu, G. Wang, Q. Dong, J. Qiu, A. Eychmüller, X. W. Lou, *Adv. Mater.* 2013, *25*, 3462; e) H. Wei, E. F. Rodriguez, A. F. Hollenkamp, A. I. Bhatt, D. H. Chen, R. A. Caruso, *Adv. Funct. Mater.* 2017, *27*, 1703270; f) Y. Zhang, Z. Y. Ding, C. W. Foster, C. E. Banks, X. Q. Qiu, X. B. Ji, *Adv. Funct. Mater.* 2017, *27*; g) P. G. Bruce, B. Scrosati, J. M. Tarascon, *Angew. Chem., Int. Ed.* 2008, *47*, 2930; h) Z. Chen, I. Belharouak, Y. K. Sun, K. Amine, *Adv. Funct. Mater.* 2013, *23*, 959; i) X. H. Gao, G. R. Li, Y. Y. Xu, Z. L. Hong, C. D. Liang, Z. Lin, *Angew. Chem., Int. Ed.* 2015, *54*, 14331; j) Y. Tang, J. Deng, W. Li, O. I. Malyi, Y. Zhang, X. Zhou, S. Pan, J. Wei, Y. Cai, Z. Chen, X. Chen, *Adv. Mater.* 2017, *29*, 1701828.

[6] a) T. C. Liu, W. G. Pell, B. E. Conway, S. L. Roberson, *J. Electrochem. Soc.* 1998, *145*, 1882; b) J. Wang, J. Polleux, J. Lim, B. Dunn, *J. Phys. Chem. C* 2007, *111*, 14925; c) C. Chen, X. Hu, Z. Wang, P. Hu, Y. Liu, Y. Huang, *Carbon* 2014, *69*, 302; d) T. Okumura, T. Fukutsuka, A. Yanagihara, Y. Orikasa, H. Arai, Z. Ogumi, Y. Uchimoto, *Chem. Mater.* 2011, *23*, 3636.

[7] a) I. E. Rauda, V. Augustyn, B. Dunn, S. H. Tolbert, *Acc. Chem. Res.* 2013, *46*, 1113; b) M. R. Lukatskaya, S. Kota, Z. Lin, M.-Q. Zhao, N. Shpigel, M. D. Levi, J. Halim, P.-L. Taberna, M. W. Barsoum, P. Simon, Y. Gogotsi, *Nat. Energy* 2017, *2*, 17105; c) V. Augustyn, J. Come, M. A. Lowe, J. W. Kim, P.-L. Taberna, S. H. Tolbert, H. D. Abruña, P. Simon, B. Dunn, *Nat. Mater.* 2013, *12*, 518; d) A. G. Dylla, G. Henkelman, K. J. Stevenson, *Acc. Chem. Res.* 2013, *46*, 1104.

[8] a) U. Lafont, D. Carta, G. Mountjoy, A. V. Chadwick, E. M. Kelder, *J. Phys. Chem. C* 2009, *114*, 1372; b) T. Okumura, T. Fukutsuka, Y. Orikasa, H. Arai, Z. Ogumi, Y. Uchimoto, *J. Mater. Chem.* 2011, *21*, 15369; c) M. Fehse, M. Ben Yahia, L. Monconduit, F. Lemoigno, M.-L. Doublet, F. Fischer, C. Tessier, L. Stievano, *J. Phys. Chem. C* 2014, *118*, 27210.

[9] a) M. F. Dupont, S. W. Donne, *J. Electrochem. Soc.* 2015, *162*, A1246; b) M. F. Dupont, S. W. Donne, *J. Electrochem. Soc.* 2016, *163*, A888; c) L. Guan, L. Yu, G. Z. Chen, *Electrochim. Acta* 2016, *206*, 464.

[10] a) K. Kang, Y. S. Meng, J. Bréger, C. P. Grey, G. Ceder, *Science* 2006, *311*, 977; b) Y.-K. Sun, D.-H. Kim, C. S. Yoon, S.-T. Myung, J. Prakash, K. Amine, *Adv. Funct. Mater.* 2010, *20*, 485; c) B. Ji, F. Zhang, M. Sheng, X. Tong, Y. Tang, *Adv. Mater.* 2017, *29*, 1604219; d) J. Wang, H. Tang, L. Zhang, H. Ren, R. Yu, Q. Jin, J. Qi, D. Mao, M. Yang, Y. Wang, P. Liu, Y. Zhang, Y. Wen, L. Gu, G. Ma, Z. Su, Z. Tang, H. Zhao, D. Wang, *Nat. Energy* 2016, *1*, 16050; e) N. Nitta, F. Wu, J. T. Lee, G. Yushin, *Mater. Today* 2015, *18*, 252; f) C. S. Rustomji, Y. Yang, T. K. Kim, J. Mac, Y. J. Kim, E. Caldwell, H. Chung, Y. S. Meng, *Science* 2017, *356*, eaal4263; g) T. Sun, Z.-J. Li, H.-G. Wang, D. Bao, F.-L. Meng, X.-B. Zhang, *Angew. Chem., Int. Ed.* 2016, *55*, 10662; h) F. Bonaccorso, L. Colombo, G. Yu, M. Stoller, V. Tozzini, A. C. Ferrari, R. S. Ruoff, V. Pellegrini, *Science* 2015, *347*, 1246501; i) J. Ji, J. Liu, L. Lai, X. Zhao, Y. Zhen, J. Lin, Y. Zhu, H. Ji, L. L. Zhang, R. S. Ruoff, *ACS Nano* 2015, *9*, 8609; j) T. Wang, R. Villegas Salvatierra, A. S. Jalilov, J. Tian, J. M. Tour, *ACS Nano* 2017, *11*, 10761; k) D. Larcher, J. M. Tarascon, *Nat. Chem.* 2015, *7*, 19; l) Y. Son, S. Sim, H. Ma, M. Choi, Y. Son, N. Park, J. Cho, M. Park, *Adv. Mater.* 2018, *30*, 1705430.

[11] a) F. Lin, Y. Liu, X. Yu, L. Cheng, A. Singer, O. G. Shpyrko, H. L. Xin, N. Tamura, C. Tian, T.-C. Weng, X.-Q. Yang, Y. S. Meng, D. Nordlund, W. Yang, M. M. Doeff, *Chem. Rev.* 2017, *117*, 13123; b) Q. F. Gu, J. A. Kimpton, H. E. A. Brand, Z. Y. Wang, S. L. Chou, *Adv. Energy Mater.* 2017, *7*, 1602831; c) M. Newville, in *Spectroscopic Methods in Mineralogy and Materials Sciences*, Vol. *78* (Eds: G. S. Henderson, D. R. Neuville, R. T. Downs), 2014, p. 33; d) Y. Du, Y. Zhu, S. Xi, P. Yang, H. O. Moser, M. B. H. Breese, A. Borgna, *J. Synchrotron Radiat.* 2015, *22*, 839; e) D. Wang, R. Kou, Y. Ren, C. J. Sun, H. Zhao, M. J. Zhang, Y. Li, A. Huq, J. Y. P. Ko, F. Pan, Y. K. Sun, Y. Yang, K. Amine, J. Bai, Z. Chen, F. Wang, *Adv. Mater.* 2017, *29*, 1606715; f) T. Petit, J. Ren, S. Choudhury, R. Golnak, S. S. N. Lalithambika, M. F. Tesch, J. Xiao, E. F. Aziz, *Adv. Mater. Interfaces* 2017, *4*, 1700755; g) Y. Ding, Z. F. Li, E. V. Timofeeva, C. U. Segre, *Adv. Energy Mater.* 2018, *8*, 1702134.

[12] K. Kirshenbaum, D. C. Bock, C.-Y. Lee, Z. Zhong, K. J. Takeuchi, A. C. Marschilok, E. S. Takeuchi, *Science* 2015, *347*, 149.
[13] U. Lafont, D. Carta, G. Mountjoy, A. V. Chadwick, E. M. Kelder, *J. Phys. Chem. C* 2010, *114*, 1372.
[14] B. Ravel, M. Newville, *J. Synchrotron Radiat.* 2005, *12*, 537.
[15] R. D. Shannon, *Acta Crystallogr., Sect. A: Cryst. Phys., Diffr., Theor. Gen. Crystallogr.* 1976, *32*, 751.
[16] a) R. Dominko, C. Sirisopanaporn, C. Masquelier, D. Hanzel, I. Arcon, M. Gaberscek, *J. Electrochem. Soc.* 2010, *157*, A1309; b) S. Kuppan, Y. Xu, Y. Liu, G. Chen, *Nat. Commun.* 2017, *8*, 14309; c) M. Pivko, I. Arcon, M. Bele, R. Dominko, M. Gaberscek, *J. Power Sources* 2012, *216*, 145.
[17] W. J. H. Borghols, D. Lützenkirchen-Hecht, W. Chan, U. Lafont, E. M. Kelder, E. R. H. van Eck, A. P. M. Kentgens, F. M. Mulder, M. Wagemaker, *J. Electrochem. Soc.* 2010, *157*, A582.
[18] a) D. W. Murphy, J. Broadhead, B. C. H. Steele, *Materials for Advanced Batteries*, Plenum Press, 1980; b) T. Kudo, M. Hibino, *Electrochim. Acta* 1998, *43*, 781; c) M. Okubo, E. Hosono, J. Kim, M. Enomoto, N. Kojima, T. Kudo, H. Zhou, I. Honma, *J. Am. Chem. Soc.* 2007, *129*, 7444.

Q9

